Electron deficient boron-doped amorphous carbon nitride to uphill N_2 photo-fixation through π back donation

Sara Ajmal [a,b], Aamir Rasheed [c], Ngoc Quang Tran [a,b], Xiaodong Shao [a,b], Yosep Hwang [a,b], Viet Q. Bui [d], Young Dok Kim [b], Jeongyong Kim [e], Hyoyoung Lee [a,b,f,*]

[a] Center for Integrated Nanostructure Physics (CINAP), Institute for Basic Science (IBS), Sungkyunkwan University, Suwon 16419, Republic of Korea
[b] Department of Chemistry, Sungkyunkwan University, Suwon 16419, Republic of Korea
[c] Department of Chemistry, University of Ulsan, Ulsan 44610, South Korea
[d] Advance Institute of Science and Technology, The University of Danang, 41 Le Duan, Danang, Vietnam
[e] Department of Energy Science, Sungkyunkwan University, Suwon 16419, Republic of Korea
[f] Department of Biophysics, Sungkyunkwan University, Suwon 16419, Republic of Korea

ARTICLE INFO

ABSTRACT

The photocatalytic Nitrogen fixation to NH_3 by using water as a protonation source is a requisite renovation for life. Albeit, the activation and adsorption of robust $N\equiv N$ is the bottleneck in NH_3 synthesis. Here, we report an amorphous-wrinkled hollow-tubular electron-deficient boron-doped carbon nitride (BCN) for improved photocatalytic N_2 fixation via "σ donation and π back donation". The electron-deficient B played synergetic roles to activate and stabilize the adsorbed N_2 i.e. (i) It tunes the bandgap of CN for effective light absorption and charge transfer; (ii) The B-N coordination site polarizes chemisorbed N_2 via electron pair acceptance; (iii) The filled sp^2 orbital of B activates the N_2 by π-back donation. Consequently, the photocatalytic performance of BCN-4 reaches $0.93 \, mmol \, h^{-1} g^{-1}$ with AQY of ~13% (350 nm) and solar to NH_3 conversion efficiency (SSC_{NH3}) of 0.017%. The in situ DRIFT and DFT studies revealed that BCN exhibited spontaneous N_2 adsorption and activation, followed by protonation of the adsorbed N_2, with a negligible energy barrier.

1. Introduction

Synthesis of Ammonia (NH_3) by reduction of atmospheric nitrogen (N_2) is the second most-produced chemical for sustaining life as well as an important carbon-free energy carrier [1,2]. Currently, the industrial Haber–Bosch (HB) process, under extreme temperatures (400–500 °C) and pressure (200–250 bar) in the presence of a metallic iron catalyst, dominates NH_3 synthesis [3]. Moreover, the HB process consumes almost 2% of global energy and needs high-purity hydrogen (from methane reforming), which is responsible for contributing greenhouse gas (CO_2) to our environment [4,5]. A CO_2-free, low temperature and pressure route for direct N_2-fixation by using earth-abundant catalysts are highly desirable for NH_3 synthesis [6,7]. Photocatalytic N_2 fixation by using water as a hydrogen source is an eco-friendly approach, as well as it does not compete with non-renewable hydrocarbon resources [8,9]. However, the high stability of the $N\equiv N$ bond (941 kJ/mol) and poor water-solubility of N_2, especially under ambient conditions, is the

bottleneck in activating as well as stabilizing N_2 molecules at the catalyst surface [10–12]. A novel tactic for adsorbing, cleaving and activating the $N\equiv N$ bond for selective nitrogen reduction is highly demanding [13,14].

The transition metals (TMs) have a unique ability to synergically accept and back-donate electrons to antibonding orbitals of N_2 due to the co-existence of occupied and unoccupied D-orbitals (Fig. 1) [15,16]. Hence, the unique electron transfer into or from the unoccupied/occupied D-orbitals will induce "amphiphilic centers" (nucleophilic base and electrophilic acid centers) that weaken the N_2 bonding [17–20]. However, protons are easier to activate at the TMs surface than N_2 due to the weaker bond strength of metal and nitrogen [21,22]. In contrast to TMs, some p-block elements such as borylene, black phosphorous, polymeric carbon nitrides and bismuth oxides might serve as an efficient photocatalyst for N_2-reduction reaction (NRR) [23–30]. Among them, carbon nitride (CN) has attracted worldwide attention for NRR due to its excellent stability, earth abundancy and easy fabrication, and

---

visible-light semiconducting nature with abundant amino functionalities that provide abundant Lewis-base sites [31–38]. Defect engineering of catalyst by doping with low valence atoms such as Calcium, Boron and Potassium generates the active centers (Lewis acid sites) to chemisorb electron-rich N_2 and meanwhile, back-donation of electrons from the filled orbital of heteroatoms to the anti-bonding orbital of N_2, weakens the $N\equiv N$ bond, thereby facilitating NRR [30,33,39]. Theoretical calculations already proved that doping of metallomimetic electron deficient 'boron' (B) in the CN might induce the Lewis-acid sites along with the Lewis-base site, i.e., "amphiphilic centers" that facilitate the $N\equiv N$ cleavage at ambient conditions [40]. Moreover, the 'B' tuned the energy bandgap of CN as well as prohibited the adsorption of protons hence it selectively adsorbed and immobilized the N_2 at CN as shown in Fig. 1b,c [41,42]. Currently, the reported NRR performances of B-doped carbon nitrides (BCN) are still far unsatisfactory due to the poor charge separation, unsatisfied active-sites as well as the use of some metal co-catalyst as the N_2 absorber [36,37,43].

Herein, we report an amorphous-wrinkled tubular electron-deficient BCN for enhancing photocatalytic N_2 fixation and its reduction to ammonia (NRR) via "σ donation and π back donation", which is an ideal NRR photocatalyst. The wrinkled tubular BCN was synthesized by a low-cost facile salt templating approach. The wrinkled morphology with many active sites available for carrying NRR and mesoporous structure for trapping the light that dramatically enhances the light absorption. The boron (B) is successfully coordinated with the 2 adjacent N atoms at the surface via N-B-N bonding. The positively charged electron-deficient B easily adsorb the π-electron-rich N_2 (Lewis's base), which is an active center for the formation of B–$N\equiv N$ bonds and inhibits the Lewis acid H^+ binding at these sites. An experimental study reveals that defects in CN are increased by increasing the boron doping, leading to a lower bandgap. Additionally, the p-type nature of Boron causes the hindrance in the recombination of the photo-generated carriers as well as facilitates visible light utilization. It is expected that under simulated sunlight irradiation, the BCN catalyst shows a high photocatalytic NRR activity to stably generate NH_3 with high Quantum efficiency and SSC_{NH3} efficiency. The DFT study is expected to elucidate that the empty orbital of sp^3 hybridized 'B' at the surface can selectively trap N_2 via BNN* linkage, also suppressing the H^+ adsorption due to the repulsion of Lewis acids. The chemisorbed N_2 * via π back donation ($*N_2 + e^- \rightarrow *N_2$) can form the $*N_2$ excited state that proceeds the protonation of $*N_2$ under

mild conditions and selectively boost ammonia formation, which supports the selective promotion of the NRR by suppressing the hydrogenation in solar light.

2. Experimental process

2.1. Synthesis of CN and BCN

CN was prepared via the salt-templating method in which a homogeneous eutectic mixture of metal chlorides was mixed with 2,4,6-trichloro-1,3,5-triazine (TCT) and pyrolyzed at a certain temperature. Briefly, TCT (0.4 mmol, Aldrich), $FeCl_3 0.6 H_2O$ (0.10 g, Aldrich.), and $CoCl_2 0.6 H_2O$ (0.19 g, Aldrich) were dissolved in 100 mL of deionized (DI) water followed by vigorous stirring for 1 h. The mixture was evaporated at 70 °C using rotavapor and kept under drying in a vacuum oven at 70 °C for 12 h. The mixture was pyrolyzed at 650 °C for 4 h in N_2 atmosphere. The obtained powder was stirred with aqua-Regia for 5 h to eliminate the metal template. The mixture was centrifuged and the obtained powder was again treated with aqua-regia to remove the template fully. Finally, the catalyst was washed with DI water (until pH 7) followed by filtration and dried in the oven overnight. BCN was also prepared using similar preparation methods except with the addition of boric acid (1 mmol, 2 mmol, 4 mmol, 6 mmol and 8 mmol) along with 2,4,6-Trichloro-1,3,5-triazine and metal chlorides mixtures followed by acid treatment, washing and drying.

2.2. Synthesis of 2D-C_3N_4

The C_3N_4 was synthesized by the already reported method. Briefly, 5 g of melamine was annealed at 500 °C at the heating rate of $3°min^{-1}$.

2.3. Synthesis of B-C_3N_4

The B-doped C_3N_4 is synthesized by adding boric acid to the melamine followed by annealing at 500 °C at the heating rate of $3°min^{-1}$.

2.4. Characterization

Powder X-ray diffraction (XRD) was performed on the Rigaku Ultima IV powder X-ray diffractometer using Cu Kα radiation (λ = 0.15418 nm)
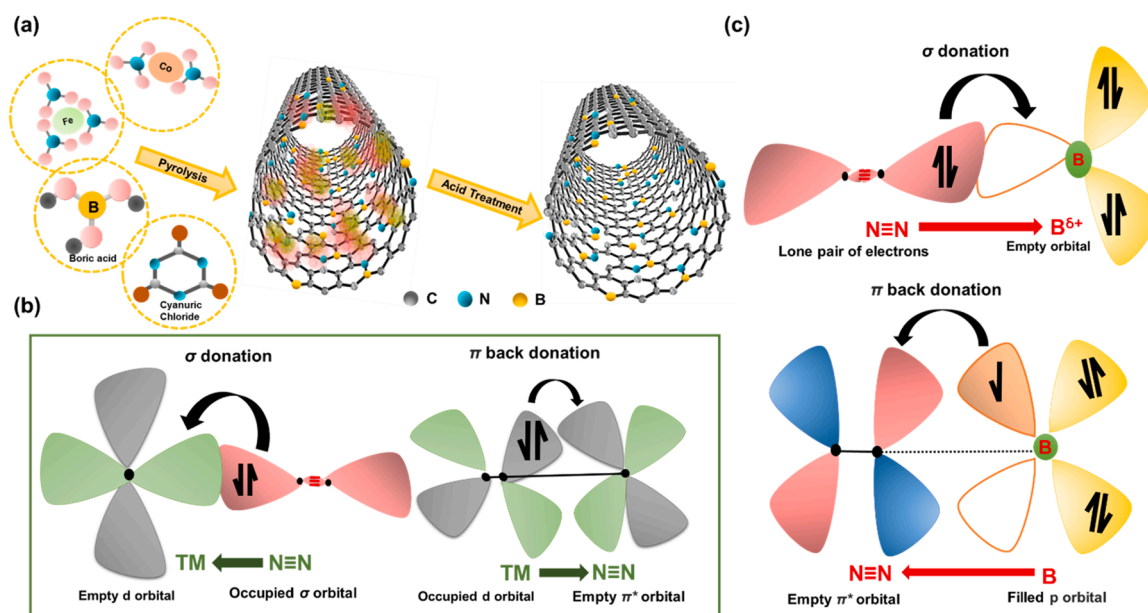

Fig. 1. a) Schematic illustration of the fabrication process of BCN. b) Schematic of N_2 adsorption and activation at transition metals. c) Schematic of N_2 adsorption and activation at BCN mimicking like transition metals (σ acceptance and π back donation).

and the Raman scattering 5 spectra were acquired at room temperature on a Horiba Jobin-Yvon Lab Ram HR VIS 6 high-resolution confocal Raman microscope with a 633 nm laser as the excitation 7 source. Scanning electron microscopy (SEM) was conducted on the JEOL 7500-F FESEM and the element maps were obtained in Oxford Instruments X-Max (INCA software) coupled to the FESEM. The transmission electron microscopy (TEM), high-angle annular dark-field scanning transmission electron microscopy (HAADF-STEM) images along with EELS mapping were obtained on a field-emission transmission 12 electron microscope (JEOL JEM 3200Fs). X-ray photoelectron spectroscopy (XPS) was conducted on Thermo VG Microtech ESCA 2000, using a monochromatic Al Kα radiation source at 100 W. The UV-Vis-NIR and DRS (diffuse reflectance spectra) were recorded on the Agilent Cary 7000. UPS analysis was performed with ESCALAB250, Thermo He–I (21.2 eV) radiation. Photoluminescence (PL) spectra were obtained by using an Agilent Cary Eclipse Fluorescence spectrometer at the wavelength of 375 nm. The time-resolved photoluminescence analysis (TRPL) was examined by laser confocal microscope (equipped with 0.9 NA objective lens), PL spectrometer and cooled charged coupled device for confocal PL (Laser beam of 375 nm and 488 nm) for acquisition time of 10 s. Ion-Chromatography (IC) for quantitative detection of NH_4^+ ions was done by Metrohm-882 compact IC plus. The BET (Brunauer–Emmett–Teller) and HK (Horvath–Kawazoe) methods were used to determine the specific surface area and sub-micropore analysis respectively by using BELSORP-max through liquid N_2 cryosorption (Micrometrics ASAP2020, USA). The size distributions were estimated by the HK and BJH (Barrett–Joyner–Halenda) methods. In-situ diffuse-reflectance FT-IR spectra were recorded using a Thermo Fisher Scientific; Nicolet-iS10 (equipped with DRIFTS accessory praying mantis, Harrick Scientific; USA) spectrophotometer at a resolution of 4 cm^{-1} in a specially designed reaction cell at room temperature. ^{1}H NMR analysis was done by BRUKER AVANCE AV(III) 500 MHz at 60scans. The ICP-AES measurements were carried out using OPTIMA 4300 DV. ICP-OES was performed on an Agilent 730. The Ammonia and Nitrogen Temperature programmed desorption analysis (TPD) was carried out by Korea Research Institute of Chemical Technology in Deajeon, Korea, AutoChem (II), Pre: He-120 ℃ for 1 hr, Ads: N_2 or NH_3 Measured Flow Rate: 50.03 cm^3 STPmin^{-1}. Room temperature Electron spin resonance (EPR) analysis was obtained from Korea Basic Science Institute in Seoul, (ESR; X-band CW-EPR, QM09) using power, microwave frequency, modulation frequency and modulation amplitude of 1 Mw, 9.64 GHz, 100 kHz and 10 G respectively. In-situ DRIFT measurements were performed using a Thermo Scientific, Nicolet Is10 FTIR spectrometer equipped with a diffuse reflectance accessory at the Infrared Spectroscopy. Each spectrum was recorded at a resolution of 2 cm^{-1} by averaging 128 scans. Thermal properties were analyzed by TGA (thermogravimetric analyzer) polymer laboratory, TGA-1000 plus.

2.5. Photo-electro-chemical experiments

The photo-electrochemical analysis was performed using a typical three-electrode cell in which the ITO glass (coated with the catalyst), saturated calomel electrode (SCE) and the platinum mesh were used as the working, reference and counter electrode respectively. The electrodes were prepared by electrophoretic deposition methods. Typically, 20 mg sample was dispersed fully in 40 mL of acetone and electrophoretic deposition was done at the constant voltage of 10 V for 5 min using Pt mesh as the counter electrode. 0.1 M Na_2SO_4 was used as the electrolyte. Before analysis, the electrolyte was saturated with N_2/Ar for 30 min. The photocurrent was measured at 0.4 V vs AgAgCl using 100 mWcm^{-2} Xenon Lamp at room temperature. The Nyquist plot was measured at the frequency range of 0.1 Hz to 100 MHz under an open circuit voltage 0.5 mV.

3. Results and discussion

3.1. Structural characterizations

The BCN nanotubes were synthesized by a salt-template method followed by acid etching (Fig. 1(a), details in the Experimental section). Firstly, the stoichiometric ratio of aqueous salts of iron and cobalt as precursors was thoroughly mixed in the TCT. Then, different amounts of 'B' precursor (1–8 mmol) were inserted into the salt/TCT, followed by stirring at 60 °C. A homogenous gel-like mixture was dried overnight, and tubular morphs were obtained after thermal treatment in an inert atmosphere at 650 °C. The porous blackish powder (Fe/Co BCN) was observed under field emission scanning electron microscopy (FESEM) (Fig. S1a, b) confirming the existence of nanotubes along with template particles with an average diameter of 8 nm. Furthermore, transmission electron microscopy (TEM) (Fig. S1c,d) confirmed the wrinkled cane-like structure. The template was subsequently removed by washing with acid and deionized (DI) water. The high-resolution SEM (Fig. 2a and S2a,b) and TEM images (Fig. S2c,d), reveal that the template has been removed from CN and the wrinkled cane-like tubular structure was preserved in the material even after acid treatment. Energy-dispersive X-ray spectroscopy (EDX) analysis confirmed the existence of B, N and C with no metal contents ratios identical to those of the g-CN (Fig. 2e-j and Table S1). The X-ray diffraction of unwashed BCN (Fig. S3) showed sharp reflections at 44.9° and 65.2° that were ascribed to the (110) and (200) planes of cubic Fe/Co template (JCPDS: 49–1567). The broad peak and less intense at ~27° (002) facet of graphitic carbon (g-CN) confirmed the interlayer-stacking of CN matrices. There was no template peak detected in the acid-treated sample, which further supports our SEM and TEM observation. Moreover, the intensity of the 002 peaks was reduced and shifted after B doping, indicating the further distortion of CN through heteroatom doping (Fig. 2k). Moreover, the TGA analysis is in Fig. S4 also confirmed the removal of the metallic template, which is well in agreement with our TEM, SEM and EDS analysis. Importantly, electron energy loss elemental mapping (EELS) acquired from the regions (Fig. 2l) further confirmed the boron doping within the CN nanotubes existence of B, C and N, which was a good agreement with the EDS analysis. To confirm the B doping FTIR (Fourier Transformed Infrared Spectroscopy) was analyzed for BCN-0 and BCN-4 in Fig. 2m. The typical C-N heterocycle stretching mode in 1200–1500 cm^{-1} and tris- triazine breathing vibrations around 800 cm^{-1} support the formation of an extended C-N-C bonding network [34,44,45]. Except for CN, an additional peak emerging at 1011 cm^{-1} was assigned to B-N stretching vibrations, confirming the successful substitution of B in the CN structure [46,47]. The increase in peak intensity of -C≡N functionalities ~2110 cm^{-1} is ascribed to the strong electron-withdrawing tendency of BCN-4 that is promising for NRR reaction [48]. The chemical bonding characteristics within the BCN materials were assessed by the high-resolution B 1 s, C 1 s, and N 1 s spectra. The representative XPS spectra of BCN-0, BCN-1, BCN-2, BCN-4, BCN-6 and BCN-8 are shown in Fig. 3. The C1s XPS of BCN-0 indicated five deconvoluted peaks positioned at 288.92, 287.1, 286.73, 285.66 and 284.6 eV (Fig. 3a), demonstrating the coexistence of N-C≡N, C-NH$_2$, C-NH$_x$, C-N and C-C bonds, respectively. After doping with 'B' in CN, the binding peaks are blue-shifted by the deviation of an extranuclear electron to the CN (electron-deficient nature of B). Hence, this asymmetric nature of B might lead to the strong adsorption of N_2 at BCN that further weakening the N≡N bonding strength.[51] The observed binding energy peaks centered at 399.1, 400.6 and 401.9 eV in N1s spectra corresponding to C-N≡C (bi-coordinated), C$_3$-N (tri-coordinated) and NH$_x$ (amino-groups), respectively (Fig. 3b). After B doping, a low binding energy peak (398.7 eV) demonstrated the existence of B-N-C bonding. Furthermore, the relative intensity of bi and tri-coordinated peaks is gradually enhanced that confirmed the reinforcement of g-CN structure by doping of B. The amino peak disappeared, which indicated the successful doping of B in the CN matrix. The relative intensity of N1s spectra
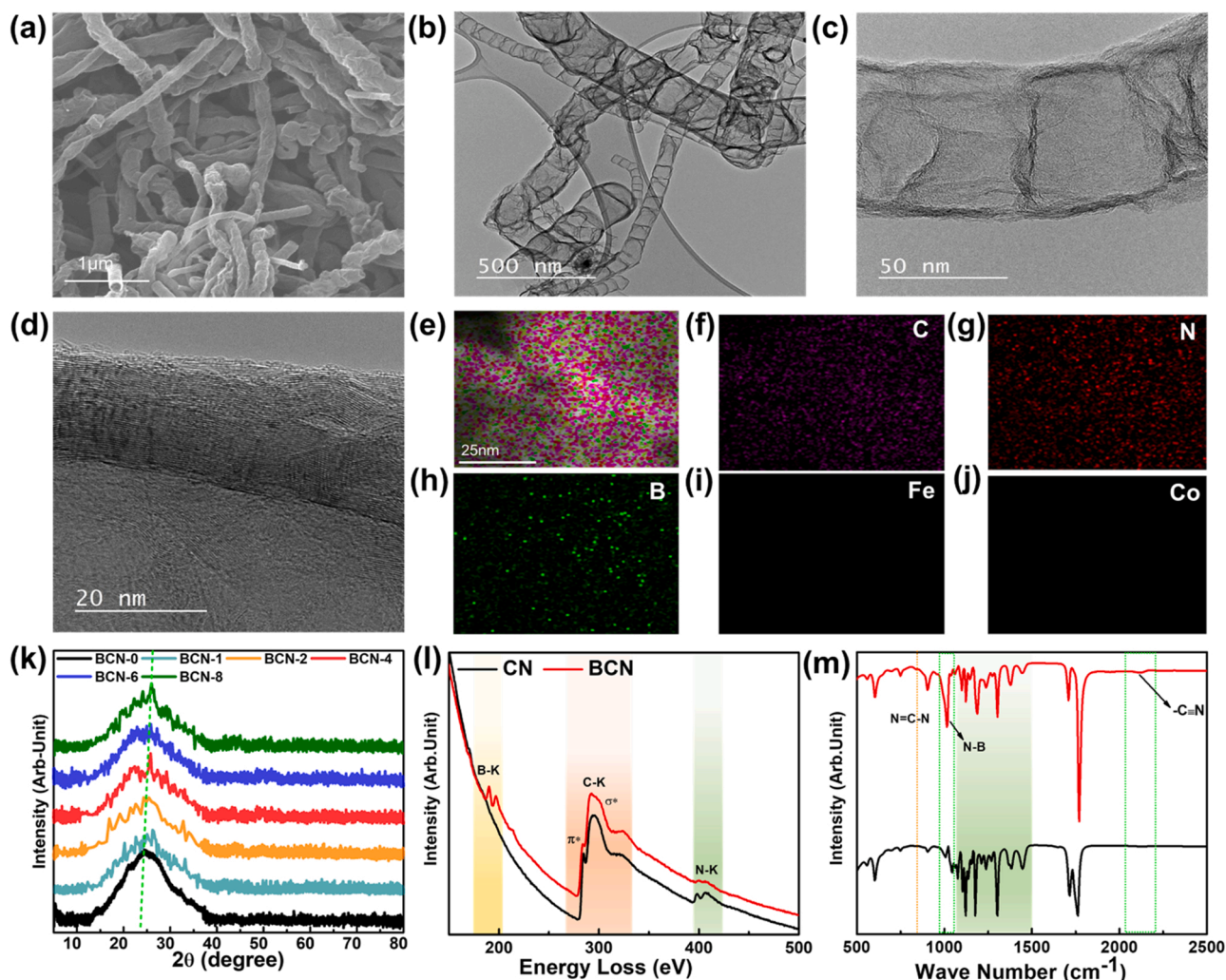
Fig. 2. a) SEM image of BCN. b-d) HRTEM image of BCN-4. e-j) EDS elemental mapping profile of BCN-4 (after washing with acid). f) C, g) N. h) B. i) Fe. j) Co. k) XRD pattern of BCN. l) EELS mapping of CN and BCN. m) FTIR of BCN-0 (black) and BCN-4 (red).

was increased until BCN-4, confirming the optimum reinforcement of g-CN structure by stabilizing N atoms at the surface. The B 1 s spectra are deconvoluted into a major peak at 190.5 eV, and a small peak at 192.5 eV (Fig. 3c), signifying the coexistence of B-N-C, and B(N)$_x$ bonds, respectively. There is no B-B binding, confirming the atomic distribution of B in CN nanotubes, typically by B-N-C and B-N coordination. The B1s peak area increased from BCN-1 to BCN-6 that further confirming the stabilization of surface N atoms of g-CN via bonding with Boron [49]. The cohabitation of electron-deficient B provides abundant electron-deficient acid-sites (B-N-C) along with base-sites (C-N) that selectively promote NRR via a "push-pull mechanism". The N$_2$ adsorption/desorption isotherms (Fig. S5) illustrated the type IV isotherm, revealing the gradual increase of specific surface area from BCN-0 to BCN-6 with randomly distributed mesopores in good agreement with XPS results. The incorporation of heteroatom (B) into CN established a large number of active sites for N$_2$ and thus improved the NRR.

3.2. Optical properties

The optical properties of BCN are examined by UV–vis, diffuse reflectance (DRS), Ultraviolet photoelectron spectroscopy (UPS) and XPS valence spectroscopy (XPS-VB). The XPS-VB and UPS analysis confirmed the valence band position of BCN gradually altered in order of BCN-0 > BCN-1 > BCN-2 > BCN4 > BCN-6 > BCN-8. The UV-Vis absorption band edge of CN was shifted to a higher wavelength (Fig. 4a)

and the bandgap was narrowed down, presumably caused by doping of 'B' (Fig. 4b). The absorption spectrum by B doping was shifted to the visible region that surprisingly mounted the light-harvesting ability as shown in Fig. S6. The UPS (Fig. 4c i) and UV–vis (Fig. 4a and S6b) revealed the more precise optical band edge and bandgap analysis of BCN-(0−8). The valance band of CN decreased by increasing the B dopant from 1.78 eV to 1.53 eV as shown in Table S2 and Fig. 4c ii. The schematic band diagram (Fig. 4d) displayed the energy band structure and redox potential of partial reactions. The energy bandgap of BCN-0, BCN-1, BCN-2, BCN-4, BCN-6 and BCN-8 was 2.6, 2.4, 2.04, 1.93, 1.75 and 1.7 eV respectively (Table S2). The continuous decline of the bandgap is due to an increase in the number of surface-defect sites on CN that tune the light absorption efficiency of the photocatalyst [50]. The N$_2$ reduction increased in the visible region by doping with B, due to the reduction of energy bandgap and suitable adjustment of band position for carrying N$_2$ reduction (details in Table S2). To evaluate the synergism of improved light-harvesting ability, and shorter surface-charge-diffusion length on the photocatalytic activity, we verify the photo-excited electron/holes (e/h) pairs recombination efficiency and surface-to charge-transfer efficiency by steady-state photoluminescence (PL) and time-resolved photoluminescence (TRPL) spectroscopy as well as electrochemical impedance spectroscopy (EIS) in BCN-0 and BCN-4. Firstly, the migration, transfer and separation efficiency of photoinduced electron-hole pairs are characterized by the PL and TRPL (Fig. 4e, f). It was demonstrated that BCN-4 showed a distinct
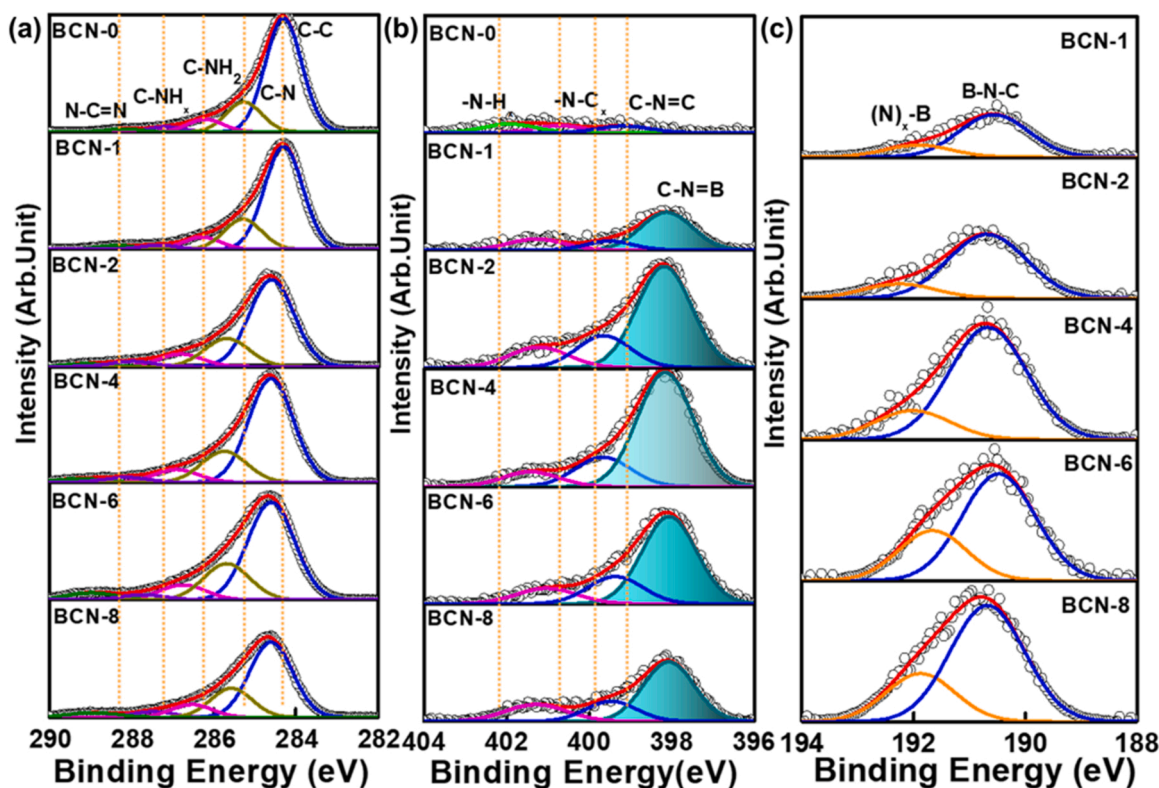
Fig. 3. Comparison of high-resolution XPS spectra of BCN-(0−8). a) C 1 s b) N 1 s c) B1s.

quenching of PL intensity compared to pristine BCN-0 (p-n junction induce built-in electric field), which favored the outstanding e/h pairs separation. The slight shift in the PL peak indicates the generation of sub-gaps due to B doping that might act as the e/h separation centers to reduce the charge recombination in BCN-4. The longer lifetime of photogenerated charge carriers confirmed the high probability of their contribution to photo-induced reactions. Hence, to investigate the lifetime of photogenerated charge carriers TRPL spectra of BCN-0 and BCN-4 were studied in Fig. 4f. The PL lifetime was calculated by fitting TRPL decay curves with the following equation;

$$PL\ Fit = y + A_1 e^{-t/t_1} + A_2 e^{-t/t_2}$$

Whereas y, A_1 and A_2 are constants corresponding to radiative and non-radiative deactivation processes while t, t_1 and t_2 are the averages, fast and slow PL decay components lifetime respectively. The average lifetime (t_{av}) is calculated by the following equation;

$$t_{av} = \frac{(B_1\ t_1^2 + B_2\ t_2^2)}{(B_1 t_1 + B_2 t_2)}$$

All of the fitted PL lifetimes are summarized in Table S3. It is confirmed that BCN-4 possessed a longer PL lifetime of (t_1 = 455 ps and t_2 = 3740 ps) compared to BCN-0 (t_1 = 342 ps and t_2 = 326 ps). The BCN-4 showed a much longer life for the majority of charge carriers at 375 nm and 488 nm. The TRPL analysis confirmed the elongation of the photogenerated charge carrier's decay time hence BCN-4 represents the higher photocatalytic activity. Therefore, the above fitting data powerfully corroborate that the lifetimes of charge carriers in CN are synergistically lengthened by boron doping. The charge mobility along with e/h separation are important factors for efficient photocatalytic reactions. The charge mobility of CN was improved by B as confirmed by photocurrent data in Fig. S6c. The BCN-4 showed the highest photocurrent (Fig. S6c), and charge transferability was observed in the "Nyquist plot" (Fig. S6f) indicating a less recombination rate and high mobility of photoinduced charge carriers in BCN-4 [51,52]. It is

concluded by the analysis of optical properties that the introduction of B moieties in CN synergistically modulates the light-harvesting ability, e/h separation efficiency and tuning of the bandgap of catalyst for improved NRR in a wide wavelength range.

3.3. Evaluation of photocatalytic NRR

The photocatalytic performance of BCN catalyst was investigated in an N_2 saturated solution using Na_2SO_3 as a sacrificial agent (SA) under a solar simulator of 100 mWcm^{-2} (1 sun) at ambient temperature. The ammonia yield was quantitatively confirmed by ion chromatography methods (Experimental detail is given in the supplementary note, Figs. S7 and S8). For comparison, the NRR performance of BCN photocatalysts with different B doping was evaluated under similar conditions. As depicted in Fig. 5a, BCN-4 attained a benchmark NRR yield of ~1.2 mmolh^{-1}g^{-1} due to excellent light absorption along with e/h separation and transferability measured by IC. The NRR performance of BCN-4 and BCN-0 is also compared with the commercial graphitic carbon nitride (C_3N_4) and B-doped C_3N_4. The wrinkled tubular CN showed even better performance than the commercial C_3N_4 and B-C_3N_4 (Fig. 5b). The wrinkled morphology of CN helped to absorb more light and transfer e/h pairs compared to the C_3N_4 and further electropositive B incorporation on CN helped to enhance the N_2 adsorption and optical band adjustment for effective NRR. To gain further insight into the efficient synthesis of ammonia from N_2, various control experiments were conducted using the best BCN-4 photocatalyst (Fig. 5c, Table S4). The results confirmed the ignorable amount of NH_4^+ ions in the Ar purged photolyte that confirmed the NRR through purged N_2. After the catalyst insertion in the photolyte, the trace amount of NH_4^+ ions was obtained in dark conditions due to some trap N_2 from the air. The NRR reaction dramatically increased in the presence of light, confirming that light and N_2 were mandatory for continuing reaction. The yield of ammonia steadily increased by increasing the concentration of SA to 3 mmol (Fig. S9a). Further increase of SA caused a decrease in NRR due
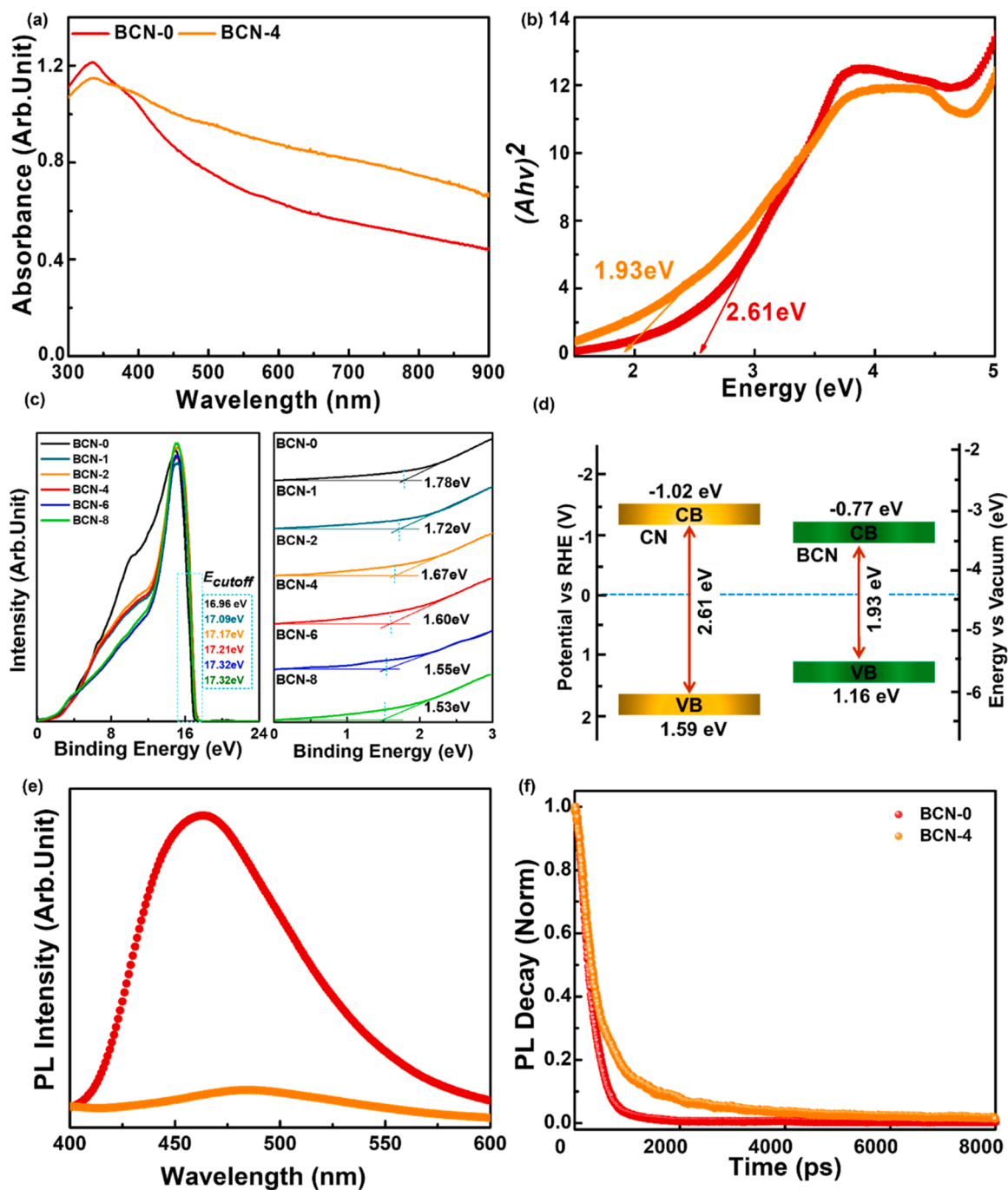
Fig. 4. Optical properties and band structures of BCN-0 and BCN-4. a) UV–visible spectra of BCN-0 and BCN-4. b) corresponding Tauc plots for BCN-0 and BCN-8. c) (i) UPS spectra of BCN-(0−8) *(The blue dotted lines indicate the E_{cutoff})* (ii) VB-spectra of BCN-(0−8). d) The band diagram for BCN-0 *(yellow)* and BCN-4 *(green)* was determined from UPS and UV–visible absorption measurements. CB, conduction band; VB, valance band. e) PL spectra of BCN-0 and BCN-4. f) TRPL spectra of BCN-0 and BCN-4.

to disturbance in the ionic balance of photolytes. The linear increase of ammonia concentration occurred with irradiation time and achieved 11.16 mmolg^{-1} within 12 h (Fig. 5d). It was observed that the initial production of ammonia was slightly higher and then decreased slightly with increasing time. The average ammonia yield was 0.93 mmolh^{-1}g^{-1} and NRR rate (0.93mmolh^{-1}g^{-1}) of BCN-4 is the highest among the previously reported carbon nitride-based photocatalysts (Table S5). To evaluate the effect of photoactivity of BCN-4 on photocatalytic NRR, the NRR performance has been assessed under different irradiation intensities and wavelengths (Fig. S10). The produced NH$_3$ amount enhanced linearly as the irradiation intensity enhanced. The light

utilization efficiency of BCN-4 was measured by AQE (Apparent quantum efficiency) by performing NRR reaction under the monochromic light source in the absence of SA. The AQE value of BCN-4 at a wavelength of 350 nm was ~13%, which was one of the highest AQE values identified in CN-based catalysts for NRR. The worthy AQE was also obtained in the visible region, confirming the large light utilization ability of the catalyst (Fig. S9 and Table S5). The solar to ammonia conversion efficiency (SSC$_{NH3}$) was measured to be 0.017%, which is comparable with the reported catalysts. It is interesting that in the absence of SA BCN-4 also exhibited a reasonable NH$_3$ production of 199μmolh^{-1}g^{-1} along with oxygen (O$_2$) production (Fig. S11), with a
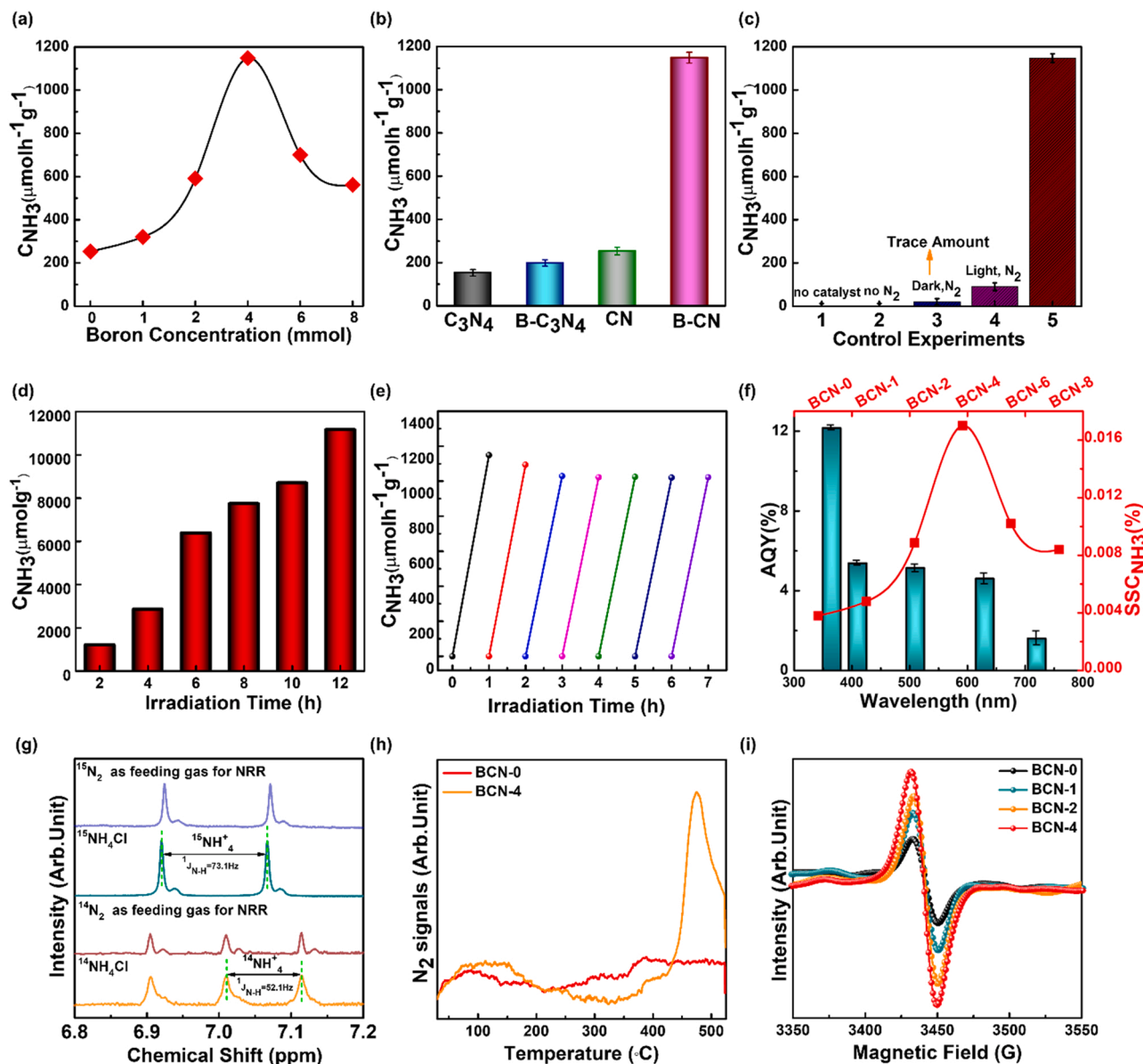
Fig. 5. Solar-driven photocatalytic NRR performance for BCN. a) Photocatalytic ammonia production rate for as prepared BCN-(0−8) in the 1-hour light irradiations conditions: 1 sun, Xenon Lamp, $NaSO_3$ as the sacrificial agent. b) Comparison of NRR performance of BCN-0 and BCN-4 with commercial 2D-C_3N_4 and B-C_3N_4 in the 1-hour light irradiations. c) Control experiment of BCN-4 irradiations under different reaction conditions (without catalyst in the presence of the sacrificial agent, light and N_2, the catalyst with no N_2 in light and no sacrificial agent, the catalyst with N_2 in the dark and sacrificial agent and catalyst with light, N_2 and Sacrificial agent). d) Time courses of Photocatalytic NRR of BCN-4. e) Cycling NRR performance of BCN-4; 1 hr light irradiation followed by Ar purging for 1 hr in dark to remove the trap N_2. f) Calculated AQY of BCN-4 in water using a monochromatic light source of 365 nm, 410 nm, 510 nm, 630 nm and 720 nm (blue) and SSC_{NH3} of BCN-(0−8) for 1 h light irradiation. g) ^1H NMR spectra of photolytes after NRR testing using $^{14}N_2$ (bottom) and $^{15}N_2$ (top) as feeding gas. h) Comparison of N_2 adsorption on the surface of BCN-0 and BCN-4 by TPD analysis, (i) Comparison of EPR spectra of BCN-0 and BCN-4.

stoichiometric ratio of NRR reaction (NH_3: O_2 2: 1.5), $N_2 + 3 H_2O \rightarrow 2NH_3 + 3/2 O_2$, confirming the consumption of photo-generated charge carriers through the water oxidation process. Hydrazine quantitative analysis was also done in the photolyte to confirm the N_2 to NH_3 selectivity in water (Fig. S12). There is no hydrazine detected in the BCN-4, proving that only ammonia was formed in the solution. The nitrate acid (HNO_3/ HNO_2) are other probable by-products that can be detected by IC as shown in Fig. S13. Highly negligible amounts of nitrates and nitrites were detected during NRR in BCN-4 (6 $\mu molh^{-1}g^{-1}$ and 0.65 $\mu molh^{-1}g^{-1}$) confirming the high selectivity of the catalyst for N_2 to NH_4^+. The durability of photocatalysts is also a vital aspect of practical application. The NRR recyclability test under 6 consecutive cycles produced the constant NH_3 yield, demonstrating efficient stability

of BCN-4 (Fig. 5e). The SEM, TEM, EDS and XPS analysis after the stability test (Fig. S14) shows no characteristic change in morphology as well as the binding energy of BCN-4. The no characteristic variation after the recyclability test confirms the excellent durability of BCN-4 under light. To further verify the NH_3 origin in BCN-4, $^{15}N_2$ isotope labeling experiment was conducted using $^{15}N_2$ as a feeding gas. The ^1H NMR spectra are in Fig. 5g depicted the duplet-distinguished peaks of $^{15}NH_4^+$, confirming that the synthesized NH_4^+ was the result of the photocatalytic reduction reaction of supplied N_2. The ^1H NMR results have been calibrated to compare the product yield of $^{15}NH_4^+$ and $^{14}NH_4^+$ with standard $^{15}NH_4Cl$ and $^{14}NH_4Cl$ solutions respectively. The concentration of $^{15}NH_4^+$ and $^{14}NH_4^+$ was almost similar (Fig. S15), which further confirmed the origin of N_2 is only the purged N_2 gas. The selective N_2

adsorption efficiency of BCN was further confirmed by temperature-programmed N_2 desorption (Fig. 5h). The wrinkled porous BCN catalyst facilitated N_2 diffusion due to a large number of electron-deficient B sites. The effect of B doping on the electronic properties of CN was studied by EPR. As shown in Fig. 5i, the EPR intensity of BCN-4 was higher than the BCN-0, confirming that the B induced the defects in the CN. The B doping caused the synergetic distribution of charge that boosted the e/h separation and light harvesting.

3.4. Photocatalytic NRR mechanism

A deeper understanding of chemical adsorption of N_2 at the catalyst surface photochemical in-situ DRIFT spectroscopic analysis was employed (details in supplementary experimental method). The spectrum clearly showed that the weak N-N adsorption peak at 1109 cm^{-1} in the presence of N_2 (dark) became more prominent in the presence of moisture (dark) and light irradiation in BCN-4, as shown in Fig. 6. It indicated that the presence of moisture promoted N_2 adsorption [48]. The OH stretching band at 3678 cm^{-1} predominantly appeared after moisture supply with N_2 [31]. The opposite band H-N-H bending
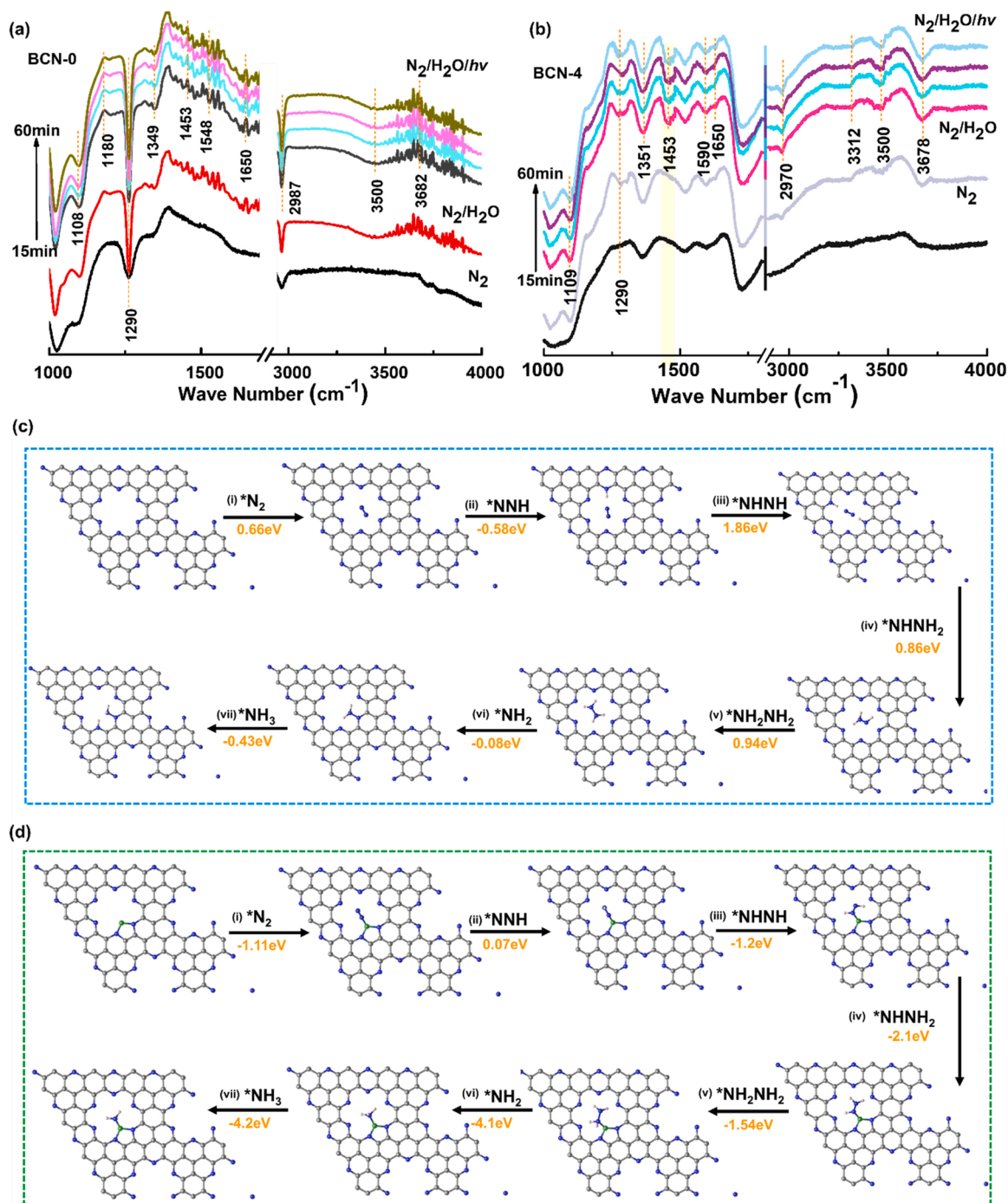

Fig. 6. a) Insitu-DRIFT spectra of BCN-0. b) Insitu-DRIFT spectra of BCN-4 (under different conditions at room temperature). c) Reaction pathway and corresponding energy changes of NRR on BCN-0. d) Reaction pathway and corresponding energy changes of NRR on BCN (C, N, H and B atoms are shown in grey, blue, pink and green colors respectively. (The * denotes the adsorption site).

vibration at 1453 cm^{-1} appeared upon light exposure in BCN-4, indicating the desorption of formed NH$_3$, which confirmed the formation of N$_2$-H$_x$ species on the catalyst surface [53]. There was no opposite band appearing in the in-situ DRIFT spectra of BCN-0 that verify the poor ammonia desorption tendency of BCN-0 than BCN-4 (Fig. 6a, b). The NH$_3$ TPD results are in Fig. S16 confirmed that BCN-0 has a good ammonia adsorption tendency as compared to BCN-4. It is difficult for BCN-0 to desorb already adsorb ammonia hence it slows down the NRR kinetics. Whereas, in BCN-4 the poor ammonia adsorption efficiency may lead to quick detachment of formed ammonia that causes the spontaneous desorption of produced ammonia from the catalyst surface. The active centers are quickly available for faster reaction kinetics in BCN-4 than in BCN-0. Moreover, in BCN-4 the peaks at 1290 cm^{-1} (NH$_2$ wagging) and 2970 cm^{-1} (strong NH stretching) become dominant with the increase of light exposure time indicating the reduction of adsorbed N$_2$ to NH$_x$. The NH$_2$ wagging (1290 cm^{-1}) peak was intense in BCN-0 compared to BCN-4 and BCN-8, confirming replacement of surface (NH$_2$) amino groups with B is well in agreement with the XPS data. In the case of BCN-8 (Fig. S17), there was no prominent difference in the intensity of functional groups upon light exposure due to the low bandgap that caused the e/h recombination. Additionally, the OH adsorption peaks (3000 cm^{-1}-3500 cm^{-1}) disappeared, indicating poor water dissociation in BCN-8 compared to BCN-0 and BCN-4 [54]. DRIFT results clearly showed the gradual increase in the intensity of the N-N adsorption peak (~1100 cm^{-1}) and decrease in the water adsorption peak (3000 cm^{-1}-3500 cm^{-1}) by increasing the 'B' concentration (0–8 mmol). It is proved that the incorporation of electron-withdrawing "B" in CN enhanced the selectivity for N$_2$ adsorption by suppressing the water adsorption (inhibiting the H$_2$ evolution) [37,55].

3.5. Theoretical insight into NRR mechanism

To elucidate the possible role of electron-deficient 'B' in accelerating the adsorption and activation of N$_2$ molecules, we further carried out DFT calculations (see details in supporting information). Based on DFT calculations in pioneering works and the calculated standard free energy diagram for the NRR in this work (Fig. S18), we proposed an enzymatic pathway, in which the hydrogenation of adsorbed N$_2$ (*N$_2$) to form *NNH species via electron-pair donation to B surface was the kinetic rate-limiting step in BCN. The further protonation steps from *NHNH to *NH$_3$ have proceeded spontaneously. Whereas, in the absence of B the second protonation is the rate-limiting step. The electron-deficient BCN reduced the Gibbs free energy (ΔG) for N$_2$ adsorption to − 1.11 eV (Fig. 6c, d). In contrast, the positive ΔG (0.66 eV) in CN indicated weak interaction for the chemisorption of N$_2$ clarifying the unsatisfactory NRR performance of CN. It was concluded that B atoms were mimicked as a transition metal and spontaneously proceeded NRR reaction via the "π * back donation-σ * donation" mechanism as shown in Fig. 1(b and c). The electron-deficient B (sp^2 orbital) accepted the lone pair electrons of N$_2$ and meanwhile, the occupied sp^2 orbitals donate electrons into the π * antibonding orbital of N$_2$. In an aqueous medium, hydrogen evolution (HER) was the competing reaction to NRR that limited the product yield and selectivity. Hence the adsorption between *H and*N$_2$ was also assessed by DFT in Fig. S19. The sluggish *H adsorption via B doping (difficult to detach) made the HER process challenging to proceed.[14, 46] In the meantime, B strengthened the N$_2$ adsorption, which was favorable for NRR also confirmed by N$_2$-TPD. To further confirm the selectivity of BCN-4 for NRR compared to HER we compared the HER performance of BCN-4 in the Ar and N$_2$ saturated environment (Fig. S20) in a fully sealed flask. It is confirmed that the presence of N$_2$ suppressed the evolution of H$_2$ due to selective adsorption of N$_2$ at the B site and adsorption of the proton by water splitting at the adsorbed at the N$_2$ * sites. Taken together, a rational construction of electron-deficient B act as a Lewis acid site that selectively adsorbed N$_2$ (Lewis's base) and forms donor-acceptor couples to promote the whole NRR process as shown in Fig. 1c. It was also found that the desorption energy of the NH$_3$ molecule decreased on the BCN (Fig. 6), indicating a rapid regeneration of the active site for new reactions. The spontaneous desorption of *NH$_3$ is due to a much stronger affinity of *NH$_3$ with OH in water than the electropositive B sites in CN.

4. Conclusion

In summary, we developed an excellent metal-free catalyst for photoconversion of N$_2$ to NH$_3$ by doping B into defect-rich wrinkled mesoporous CN. Our investigations revealed that the wrinkled mesoporous tubular electron-deficient BCN played a pivotal role in regulating the band structures for promoting light harvesting and inhibiting e/h recombination. The B doping induced multi-synergetic effects of selective N$_2$ activation and dissociation by tailoring the Lewis acid-base sites in CN. The experimental and theoretical results confirmed that the built-in B-N site was a catalytically valid active center to chemisorb N$_2$ by electron pair acceptance (σ-donation) and the filled sp^2 orbital of 'B' back-donate electrons to the anti-bonding π * orbital of N$_2$. The BCN exhibited an outstanding NH$_3$ production rate and photochemical stability, which was superior to all the reported CN-based catalysts. The ammonia production rate of BCN-4 reached 0.93 mmolh^{-1}g^{-1} with an AQY of 12% (350 nm). Our work opens a new avenue for tuning the band structure of cost-effective CN via doping with other non-metal elements towards standout NRR under ambient conditions.

Declaration of Competing Interest

The authors declare that they have no known competing financial interests or personal relationships that could have appeared to influence the work reported in this paper.

Data Availability

The data that support the findings of this study are available in the supplementary material of this article.

Appendix A. Supporting information

Supplementary data associated with this article can be found in the online version at doi:10.1016/j.apcatb.2022.122070.

References

[1] J.S. Anderson, J. Rittle, J.C. Peters, Catalytic conversion of nitrogen to ammonia by an iron model complex, Nature 501 (2013) 84–87, https://doi.org/10.1038/nature12435.

[2] J. Yao, J. Yan, Interfacial polarization triggered by single atoms boosts N_2 electroreduction, Chem 6 (2020) 808–810, https://doi.org/10.1016/j.chempr.2020.03.013.

[3] J.W. Erisman, M.A. Sutton, J. Galloway, Z. Klimont, W. Winiwarter, How a century of ammonia synthesis changed the world, Nat. Geosci. 1 (2008) 636–639, https://doi.org/10.1038/ngeo325.

[4] I. Rafiqul, C. Weber, B. Lehmann, A. Voss, Energy efficiency improvements in ammonia production—perspectives and uncertainties, Energy 30 (2005) 2487–2504, https://doi.org/10.1016/j.energy.2004.12.004.

[5] K.-i Aika, L. Christiansen, I. Dybkjaer, J. Hansen, P.H. Nielsen, A. Nielsen, P. Stoltze, K. Tamaru, Ammonia: Catalysis and Manufacture, Springer Science & Business Media, 2012.

[6] B.H. Suryanto, H.-L. Du, D. Wang, J. Chen, A.N. Simonov, D.R. MacFarlane, Challenges and prospects in the catalysis of electroreduction of nitrogen to ammonia, Nat. Catal. 2 (2019) 290–296, https://doi.org/10.1016/j.xcrp.2021.100438.

[7] J.N. Galloway, A.R. Townsend, J.W. Erisman, M. Bekunda, Z. Cai, J.R. Freney, L. A. Martinelli, S.P. Seitzinger, M.A. Sutton, Transformation of the nitrogen cycle: recent trends, questions, and potential solutions, Science 320 (2008) 889–892, https://doi.org/10.1126/science.1136674.

[8] C. Mao, J. Wang, Y. Zou, G. Qi, J.Y. Yang Loh, T. Zhang, M. Xia, J. Xu, F. Deng, M. Ghoussoub, Hydrogen spillover to oxygen vacancy of TiO2–x H y/Fe: breaking the scaling relationship of ammonia synthesis, J. Am. Chem. Soc. 142 (2020) 17403–17412, https://doi.org/10.1021/jacs.0c06118.

[9] N. Dhar, N. Pant, Nitrogen loss from soils and oxide surfaces, Nature 153 (1944) 115–116, https://doi.org/10.1038/153115a0.

[10] K.C. MacLeod, D.J. Vinyard, P.L. Holland, A multi-iron system capable of rapid N_2 formation and N_2 cleavage, J. Am. Chem. Soc. 136 (2014) 10226–10229, https://doi.org/10.1021/ja505193z.

[11] H. Li, J. Shang, Z. Ai, L. Zhang, Efficient visible light nitrogen fixation with BiOBr nanosheets of oxygen vacancies on the exposed {001} facets, J. Am. Chem. Soc. 137 (2015) 6393–6399, https://doi.org/10.1021/jacs.5b03105.

[12] J. Li, P. Liu, Y. Tang, H. Huang, H. Cui, D. Mei, C. Zhong, Single-atom Pt–N3 sites on the stable covalent triazine framework nanosheets for photocatalytic N_2 fixation, ACS Catal. 10 (2020) 2431–2442, https://doi.org/10.1021/acscatal.9b04925.

[13] A. Singh, B. Rohr, J. Schwalbe, M. Cargnello, K. Chan, T. Jaramillo, I. B. Chorkendorff, J.K. Nørskov, Electrochemical ammonia synthesis—the selectivity challenge, ACS Catal. 7 (2017) 706–709, https://doi.org/10.1021/acscatal.6b03035.

[14] X. Guo, J. Gu, S. Lin, S. Zhang, Z. Chen, S. Huang, Tackling the activity and selectivity challenges of electrocatalysts toward the nitrogen reduction reaction via atomically dispersed biatom catalysts, J. Am. Chem. Soc. 142 (2020) 5709–5721, https://doi.org/10.1021/jacs.9b13349.

[15] Z.-H. Xue, S.-N. Zhang, Y.-X. Lin, H. Su, G.-Y. Zhai, J.-T. Han, Q.-Y. Yu, X.-H. Li, M. Antonietti, J.-S. Chen, Electrochemical reduction of N_2 into NH3 by donor–acceptor couples of Ni and Au nanoparticles with a 67.8% Faradaic efficiency, J. Am. Chem. Soc. 141 (2019) 14976–14980, https://doi.org/10.1021/jacs.9b07963.

[16] X. Shao, M. Liang, A. Kumar, X. Liu, H. Jin, S. Ajmal, V.Q. Bui, H.T.D. Bui, J. Lee, N.Q. Tran, Amorphization of metal nanoparticles by 2D twisted polymer for super hydrogen evolution reaction, Adv. Energy Mater. 12 (2022) 2102257, https://doi.org/10.1002/aenm.202102257.

[17] J. Wang, L. Yu, L. Hu, G. Chen, H. Xin, X. Feng, Ambient ammonia synthesis via palladium-catalyzed electrohydrogenation of dinitrogen at low overpotential, Nat. Commun. 9 (2018) 1–7, https://doi.org/10.1038/s41467-018-04213-9.

[18] R.J. Burford, M.D. Fryzuk, Examining the relationship between coordination mode and reactivity of dinitrogen, Nat. Rev. Chem. 1 (2017) 1–13, https://doi.org/10.1038/s41570-017-0026.

[19] N. Zhang, A. Jalil, D. Wu, S. Chen, Y. Liu, C. Gao, W. Ye, Z. Qi, H. Ju, C. Wang, Refining defect states in $W_{18}O_{49}$ by Mo doping: a strategy for tuning n_2 activation towards solar-driven nitrogen fixation, J. Am. Chem. Soc. (2018) https://doi.org/10.1021/jacs.8b02076.

[20] M.-H. Vu, M. Sakar, C.-C. Nguyen, T.-O. Do, Chemically bonded Ni cocatalyst onto the S doped g-C3N4 nanosheets and their synergistic enhancement in H2 production under sunlight irradiation, ACS Sustain. Chem. Eng. 6 (2018) 4194–4203, https://doi.org/10.1021/acssuschemeng.7b04598.

[21] X. Xue, R. Chen, H. Chen, Y. Hu, Q. Ding, Z. Liu, L. Ma, G. Zhu, W. Zhang, Q. Yu, Oxygen vacancy engineering promoted photocatalytic ammonia synthesis on ultrathin two-dimensional bismuth oxybromide nanosheets, Nano Lett. 18 (2018) 7372–7377, https://doi.org/10.1021/acs.nanolett.8b03655.

[22] Y. Ren, C. Yu, X. Tan, H. Huang, Q. Wei, J. Qiu, Strategies to suppress hydrogen evolution for highly selective electrocatalytic nitrogen reduction: challenges and perspectives, Energy Environ. Sci. 14 (2021) 1176–1193, https://doi.org/10.1039/D0EE03596C.

[23] F. Köleli, T. Röpke, Electrochemical hydrogenation of dinitrogen to ammonia on a polyaniline electrode, Appl. Catal. B: Environ. 62 (2006) 306–310, https://doi.org/10.1016/j.apcatb.2005.08.006.

[24] Q. Wang, Y. Lei, D. Wang, Y. Li, Defect engineering in earth-abundant electrocatalysts for CO 2 and N 2 reduction, Energy Environ. Sci. 12 (2019) 1730–1750, https://doi.org/10.1039/C8EE03781G.

[25] S. Bian, M. Wen, J. Wang, N. Yang, P.K. Chu, X.-F. Yu, Edge-rich black phosphorus for photocatalytic nitrogen fixation, J. Phys. Chem. Lett. 11 (2020) 1052–1058, https://doi.org/10.1021/acs.jpclett.9b03507.

[26] Z.-K. Shen, Y.-J. Yuan, P. Wang, W. Bai, L. Pei, S. Wu, Z.-T. Yu, Z. Zou, ACS Appl. Mater. Interfaces 12 (2020) 17343–17352, https://doi.org/10.1021/acsami.9b21167.

[27] P. Qiu, C. Xu, N. Zhou, H. Chen, F. Jiang, Metal-free black phosphorus nanosheets-decorated graphitic carbon nitride nanosheets with CP bonds for excellent photocatalytic nitrogen fixation, Appl. Catal. B Environ. 221 (2018) 27–35, https://doi.org/10.1016/J.APCATB.2017.09.010.

[28] Y. Wan, H. Zhou, M. Zheng, Z.H. Huang, F. Kang, J. Li, R. Lv, Oxidation state modulation of bismuth for efficient electrocatalytic nitrogen reduction to ammonia, Adv. Funct. Mater. 31 (2021) 2100300, https://doi.org/10.1002/adfm.202100300.

[29] C. Lv, L. Zhong, Y. Yao, D. Liu, Y. Kong, X. Jin, Z. Fang, W. Xu, C. Yan, K.N. Dinh, Boosting electrocatalytic ammonia production through mimicking "π back-donation", Chem 6 (2020) 2690–2702, https://doi.org/10.1016/j.chempr.2020.07.006.

[30] M.-A. Légaré, G. Bélanger-Chabot, R.D. Dewhurst, E. Welz, I. Krummenacher, B. Engels, H. Braunschweig, Nitrogen fixation and reduction at boron, Science 359 (2018) 896–900, https://doi.org/10.1126/science.aaq1684.

[31] D. Hao, C. Liu, X. Xu, M. Kianinia, I. Aharonovich, X. Bai, X. Liu, Z. Chen, W. Wei, G. Jia, Surface defect-abundant one-dimensional graphitic carbon nitride nanorods boost photocatalytic nitrogen fixation, New J. Chem. 44 (2020) 20651–20658, https://doi.org/10.1039/D0NJ04068A.

[32] S. Ajmal, H.T. Bui, V.Q. Bui, T. Yang, X. Shao, A. Kumar, S.-G. Kim, H. Lee, Accelerating water reduction towards hydrogen generation via cluster size adjustment in Ru-incorporated carbon nitride, Chem. Eng. J. 429 (2022), 132282, https://doi.org/10.1016/j.cej.2021.132282.

[33] W. Wang, H. Zhang, S. Zhang, Y. Liu, G. Wang, C. Sun, H. Zhao, Potassium-ion-assisted regeneration of active cyano groups in carbon nitride nanoribbons: visible-light-driven photocatalytic nitrogen reduction, Angew. Chem. Int. Ed. 58 (2019) 16644–16650, https://doi.org/10.1002/anie.201908640.

[34] C. Liang, H.-Y. Niu, H. Guo, C. Niu, D. Huang, Y.-Y. Yang, H.-Y. Liu, B. Shao, H. Feng, Insight into photocatalytic nitrogen fixation on graphitic carbon nitride: Defect-dopant strategy of nitrogen defect and boron dopant, Chem. Eng. J. 396 (2020), 125395, https://doi.org/10.1007/s12274-021-3725-0.

[35] G. Peng, J. Wu, M. Wang, J. Niklas, H. Zhou, C. Liu, Nitrogen-defective polymeric carbon nitride nanolayer enabled efficient electrocatalytic nitrogen reduction with high faradaic efficiency, Nano Lett. 20 (2020) 2879–2885, https://doi.org/10.1021/acs.nanolett.0c00698.

[36] Y. Shiraishi, Y. Shiota, Y. Kofuji, M. Hashimoto, K. Chishiro, H. Hirakawa, S. Tanaka, S. Ichikawa, T. Hirai, Nitrogen fixation with water on carbon-nitride-based metal-free photocatalysts with 0.1% solar-to-ammonia energy conversion efficiency, ACS Appl. Energy Mater. 1 (2018) 4169–4177, https://doi.org/10.1021/acsaem.8b00829.

[37] Y. Shiraishi, K. Chishiro, S. Tanaka, T. Hirai, Photocatalytic dinitrogen reduction with water on boron-doped carbon nitride loaded with nickel phosphide particles, Langmuir 36 (2020) 734–741, https://doi.org/10.1021/acs.langmuir.9b03445.

[38] Z.-Q. Chu, C. Stampfl, X.-M. Duan, Boron-Doped g-C6N6 layer as a metal-free photoelectrocatalyst for N_2 reduction reaction, J. Phys. Chem. C. 123 (2019) 28739–28743, https://doi.org/10.1021/acs.jpcc.9b08169.

[39] B. Rösch, T.X. Gentner, Dinitrogen complexation and reduction at low-valent calcium, Science 371 (2021) 1125–1128, https://doi.org/10.1126/science.abf2374.

[40] M.-A. Légaré, C. Pranckevicius, H. Braunschweig, Metallomimetic chemistry of boron, Chem. Rev. 119 (2019) 8231–8261, https://doi.org/10.1021/acs.chemrev.8b00561.

[41] L. Jasin Arachchige, Y. Xu, Z. Dai, X. Zhang, F. Wang, C. Sun, Theoretical investigation of single and double transition metals anchored on graphyne monolayer for nitrogen reduction reaction, J. Phys. Chem. C. 124 (2020) 15295–15301, https://doi.org/10.1021/acs.jpcc.0c03899.

[42] X. Lv, W. Wei, F. Li, B. Huang, Y. Dai, Metal-Free B@g-CN: visible/infrared light-driven single atom photocatalyst enables spontaneous dinitrogen reduction to ammonia, Nano Lett. 19 (2019) 6391–6399, https://doi.org/10.1021/acs.nanolett.9b02572.

[43] Y. Ran, X. Yu, J. Liu, J. Cui, J. Wang, L. Wang, Y. Zhang, X. Xiang, J. Ye, Polymeric carbon nitride with frustrated Lewis pair sites for enhanced photofixation of nitrogen, J. Mater. Chem. A 8 (2020) 13292–13298, https://doi.org/10.1039/D0TA03914D.

[44] Z. Lin, X. Wang, Nanostructure engineering and doping of conjugated carbon nitride semiconductors for hydrogen photosynthesis, Angew. Chem. 125 (2013) 1779–1782, https://doi.org/10.1002/anie.201209017.

[45] S. Wang, L. Zhang, Z. Xia, A. Roy, D.W. Chang, J.B. Baek, L. Dai, BCN graphene as efficient metal-free electrocatalyst for the oxygen reduction reaction, Angew. Chem. Int. Ed. 51 (2012) 4209–4212, https://doi.org/10.1002/anie.201109257.

[46] D. Gao, Y. Liu, P. Liu, M. Si, D. Xue, Atomically thin B doped g-C3N4 nanosheets: high-temperature ferromagnetism and calculated half-metallicity, Sci. Rep. 6 (2016) 1–8, https://doi.org/10.1038/srep35768.

[47] X. Yu, P. Han, Z. Wei, L. Huang, Z. Gu, S. Peng, J. Ma, G. Zheng, Boron-doped graphene for electrocatalytic N_2 reduction, Joule 2 (2018) 1610–1622, https://doi.org/10.1016/j.joule.2018.06.007.

[48] Y. Cui, Z. Ding, X. Fu, X. Wang, Construction of conjugated carbon nitride nanoarchitectures in solution at low temperatures for photoredox catalysis, Angew. Chem. Int. Ed. 51 (2012) 11814–11818, https://doi.org/10.1002/anie.201206534.

[49] J. Qu, Q. Li, C. Luo, J. Cheng, X. Hou, Characterization of flake boron nitride prepared from the low temperature combustion synthesized precursor and its application for dye adsorption, Coatings 8 (2018) 214, https://doi.org/10.3390/coatings8060214.

[50] S. Hu, F. Li, Z. Fan, F. Wang, Y. Zhao, Z. Lv, Band gap-tunable potassium doped graphitic carbon nitride with enhanced mineralization ability, Dalton Trans. 44 (2015) 1084–1092, https://doi.org/10.1039/C4DT02658F.

[51] Z. Zhang, J.T. Yates Jr, Band bending in semiconductors: chemical and physical consequences at surfaces and interfaces, Chem. Rev. 112 (2012) 5520–5551, https://doi.org/10.1021/cr3000626.

[52] D. Zhao, Y. Wang, C.-L. Dong, Y.-C. Huang, J. Chen, F. Xue, S. Shen, L. Guo, Boron-doped nitrogen-deficient carbon nitride-based Z-scheme heterostructures for photocatalytic overall water splitting, Nat. Energy 6 (2021) 388–397, https://doi.org/10.1038/s41560-021-00795-9.

[53] G. Zhang, H. Xu, Y. Li, C. Xiang, Q. Ji, H. Liu, J. Qu, J. Li, Interfacial engineering of SeO ligands on tellurium featuring synergistic functionalities of bond activation and chemical states buffering toward electrocatalytic conversion of nitrogen to ammonia, Adv. Sci. 6 (2019) 1901627, https://doi.org/10.1002/advs.201901627.

[54] Y. Yao, S. Zhu, H. Wang, H. Li, M. Shao, A spectroscopic study on the nitrogen electrochemical reduction reaction on gold and platinum surfaces, J. Am. Chem. Soc. 140 (2018) 1496–1501, https://doi.org/10.1021/jacs.7b12101.

[55] J. Liu, M.S. Kelley, W. Wu, A. Banerjee, A.P. Douvalis, J. Wu, Y. Zhang, G.C. Schatz, M.G. Kanatzidis, Nitrogenase-mimic iron-containing chalcogels for photochemical reduction of dinitrogen to ammonia, Proc. Nation Acad. Sci. 113 (2016) 5530–5535, https://doi.org/10.1073/pnas.1605512113.